Single-Atom Catalysts

International Edition: DOI: 10.1002/anie.201701089
German Edition: DOI: 10.1002/ange.201701089

Supported Rhodium Catalysts for Ammonia–Borane Hydrolysis: Dependence of the Catalytic Activity on the Highest Occupied State of the Single Rhodium Atoms

Liangbing Wang[+], Hongliang Li[+], Wenbo Zhang, Xiao Zhao, Jianxiang Qiu, Aowen Li, Xusheng Zheng, Zhenpeng Hu, Rui Si,* and Jie Zeng**

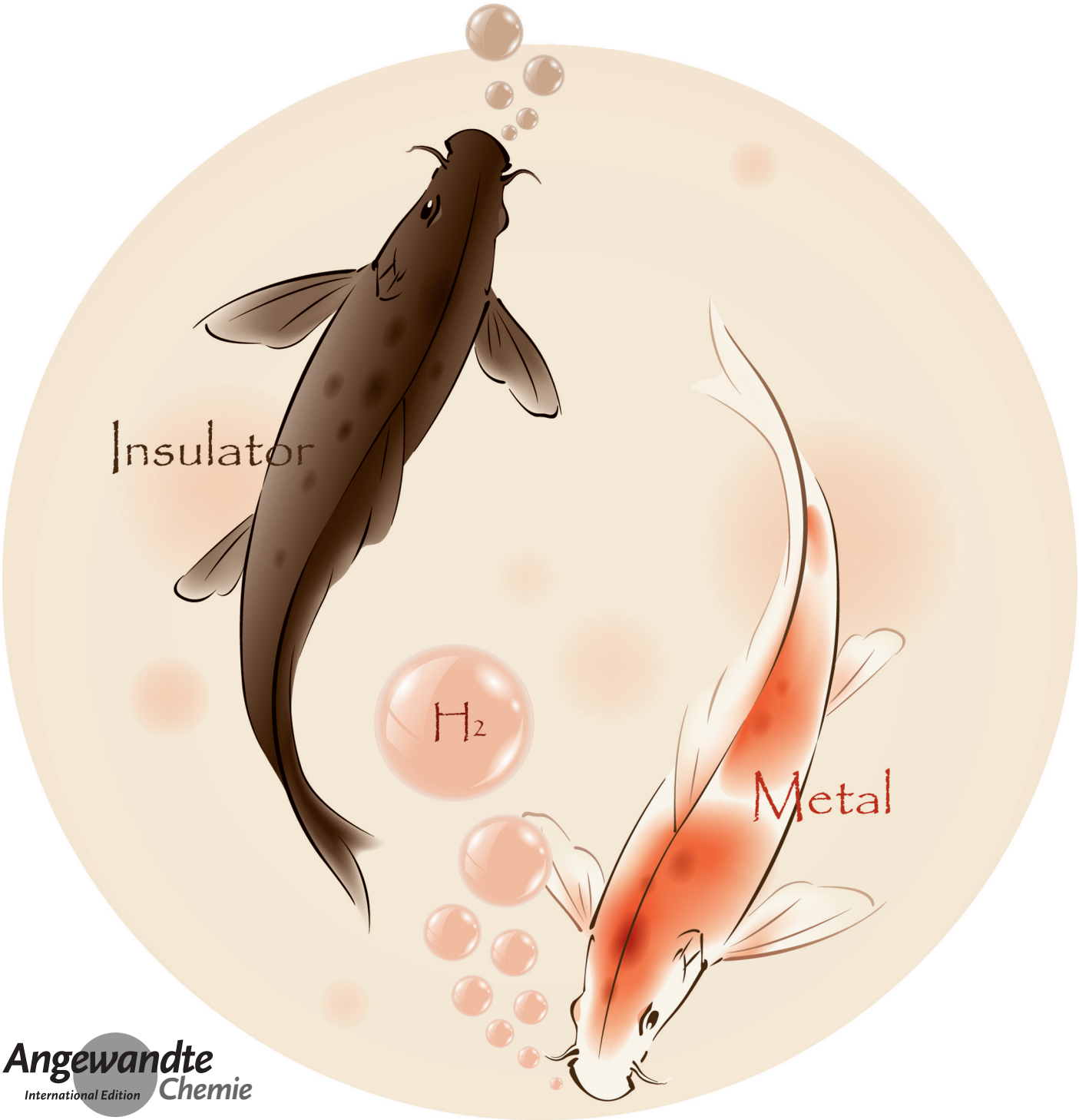

Abstract: *Supported metal nanocrystals have exhibited remarkable catalytic performance in hydrogen generation reactions, which is influenced and even determined by their supports. Accordingly, it is of fundamental importance to determine the direct relationship between catalytic performance and metal–support interactions. Herein, we provide a quantitative profile for exploring metal–support interactions by considering the highest occupied state in single-atom catalysts. The catalyst studied consisted of isolated Rh atoms dispersed on the surface of VO_2 nanorods. It was observed that the activation energy of ammonia–borane hydrolysis changed when the substrate underwent a phase transition. Mechanistic studies indicate that the catalytic performance depended directly on the highest occupied state of the single Rh atoms, which was determined by the band structure of the substrates. Other metal catalysts, even with non-noble metals, that exhibited significant catalytic activity towards NH_3BH_3 hydrolysis were rationally designed by adjusting their highest occupied states.*

Hydrogen generation from chemical hydrogen storage materials in a catalytic process is a convenient, inexpensive, and effective approach to apply hydrogen energy in a practical fashion.[1] Typical hydrogen storage chemicals include formic acid (HCOOH), hydrous hydrazine ($N_2H_4{\cdot}H_2O$), methanol (CH_3OH), and ammonia–borane (NH_3BH_3), with hydrogen contents of 4.4, 8.0, 18.8, and 19.6 wt%, respectively.[2–6] Finding efficient catalysts towards H_2 release from these materials under mild conditions is urgently required. Thanks to extensive efforts, supported metal nanocrystals have been reported to display remarkable catalytic performance, which was found to be significantly influenced and even determined by their supports.[6–11] Accordingly, determining the relationship between catalytic performance and metal–support interactions is of fundamental importance. However, it remains challenging to quantitatively understand the nature of metal–support interactions owing to the lack of detailed knowledge of reaction processes in hydrolysis reactions and active sites at the atomic level. Specifically, the well-established reaction paths of hydrolysis reactions under homogeneous catalysis cannot be directly applied to heterogeneous catalysis because of the existence of a phase interface and complex active sites in heterogeneous catalysis.[3–5] The details of the reaction process of NH_3BH_3 hydrolysis over solid catalysts have not been determined experimentally. Density functional theory (DFT) calculations were conducted to gain insight into the reaction path but the theoretical energy barrier was much higher than the experimental activation energy.[12] As for the exact active sites in this reaction, preliminary mechanistic studies suggested that the hydrolysis reaction occurred at the interface of metal and support, whereas some studies attributed the activity to the surface of the metal nanocrystals.[7–10]

To solve the aforementioned problems, state-of-the-art single-atom catalysts have been proposed as an ideal platform to investigate metal–support interactions because interference from the size, shape, and orientation of the metal particles at the metal–support interface can be readily excluded.[13,14] Moreover, phase-transition materials are regarded as suitable supports for single atoms to reveal the key role of metal–support interactions in the catalysis process, as the band structure of the substrate can be modulated while keeping the spatial distribution of the single atoms, and thus the active sites, unchanged. One of the most widely studied materials in this area is vanadium dioxide (VO_2), which undergoes a metal–insulator phase transition at approximately 341.0 K.[15]

Herein, we provide a quantitative approach for exploring metal–support interactions by considering the highest occupied state in single-atom catalysts. The single-atom catalyst consisted of isolated Rh atoms uniformly dispersed on the surface of VO_2 nanorods (denoted as Rh_1/VO_2). During NH_3BH_3 hydrolysis, changes in the activation energy were induced by phase transitions of the substrate. Further experimental analysis and DFT calculations indicate that the catalytic performance directly correlates with the highest occupied state of the individual Rh atoms, which in turn depends on the band structure of the substrate. Based on the aforementioned reaction mechanism, other metal catalysts, even with non-noble metals, that exhibit significant catalytic activity towards NH_3BH_3 hydrolysis were rationally designed by adjusting their highest occupied states.

First, VO_2 nanorods in the monoclinic phase were synthesized with an average diameter of 240 nm (see the Supporting Information, Figure S1). Owing to the fully reversible phase transition between monoclinic VO_2(M) and rutile VO_2(R), these VO_2 nanorods underwent a typical metal–insulator transition at approximately 341.0 K as revealed by the changes in the resistance as a function of temperature (Figure S2 A), with a transition region of 337.2–344.2 K. We prepared single-atom Rh_1/VO_2 catalysts by simply injecting Na_3RhCl_6 solution into an aqueous solution containing VO_2 nanorods, followed by stirring at 300 rpm at room temperature for 1 h. In this process, the Rh^{3+} ions in the Na_3RhCl_6 solution are reduced to Rh^+ by V^{4+} in the VO_2 nanorods as the average molar ratio of leached V species to supported Rh single atoms was determined to be 2.1 (see the

[*] L. Wang,[+] H. Li,[+] W. Zhang, X. Zhao, J. Qiu, A. Li, X. Zheng, Prof. J. Zeng
Hefei National Laboratory for Physical Sciences at the Microscale
Key Laboratory of Strongly-Coupled Quantum Matter Physics of Chinese Academy of Sciences
Department of Chemical Physics
University of Science and Technology of China
Hefei, Anhui 230026 (P.R. China)
E-mail: zengj@ustc.edu.cn
Prof. Z. Hu
School of Physics, Nankai University
Tianjin 300071 (P.R. China)
E-mail: zphu@nankai.edu.cn
Prof. R. Si
Shanghai Synchrotron Radiation Facility
Shanghai Institute of Applied Physics
Chinese Academy of Sciences
Shanghai 201204 (P.R. China)
E-mail: sirui@sinap.ac.cn
[+] These authors contributed equally to this work.

Supporting information for this article can be found under: http://dx.doi.org/10.1002/anie.201701089.

Experimental Section in the Supporting Information). The Rh mass loading was determined to be 0.5% by inductively coupled plasma atomic emission spectroscopy (ICP-AES). The electric properties of Rh_1/VO_2 are similar to those of VO_2 (Figure S2B). Figure 1A shows a high-angle annular dark-field scanning transmission electron microscopy (HAADF-STEM) image of Rh_1/VO_2. Individual Rh atoms, which were observed as bright spots and marked with white circles, were uniformly dispersed on the surface of the VO_2 nanorods. Further analysis of a magnified HAADF-STEM image of Rh_1/VO_2 shows that the Rh atoms exactly occupied the positions of V atoms (Figure 1B). The intensity profile (Figure 1C) along the X-Y line in Figure 1B corroborates the presence of isolated Rh atoms as the signal intensity is approximately proportional to the square of the atomic number.[16]

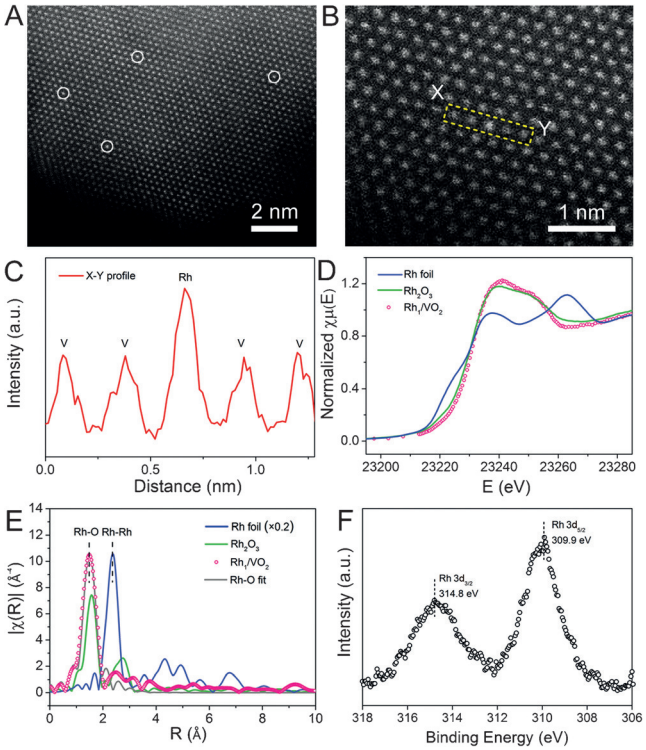

Figure 1. A) HAADF-STEM and B) magnified HAADF-STEM images of Rh_1/VO_2. C) Intensity profile along the X–Y line in (B). D) Rh K-edge XANES spectra for Rh_1/VO_2, Rh_2O_3, and Rh foil. E) Rh K-edge EXAFS spectra in R space for Rh_1/VO_2 with the corresponding fitted curve, Rh_2O_3, and Rh foil. F) XPS spectrum of Rh 3d for Rh_1/VO_2.

The X-ray absorption near-edge spectroscopy (XANES) and extended X-ray absorption fine structure (EXAFS) profiles were recorded to determine the electronic structure and coordination of the Rh atoms in Rh_1/VO_2. The XANES profile of Rh_1/VO_2 is similar to that of Rh_2O_3 (Figure 1D), revealing that the Rh species in Rh_1/VO_2 were present in an oxidized state. As shown by the EXAFS spectrum in R space (Figure 1E), Rh_1/VO_2 exhibited a prominent peak at approximately 2.0 Å from the Rh–O shell with a coordination number of 6.4 (Table S1). No other typical peaks for Rh–Rh contributions at longer distances (>2.0 Å) were observed, revealing the dispersion of isolated Rh atoms throughout the whole Rh_1/VO_2 structure, which is consistent with the HAADF-STEM data. To further characterize the electronic properties of Rh_1/VO_2, we conducted X-ray photoelectron spectroscopy (XPS) measurements. In general, the binding energy of Rh $3d_{5/2}$ for Rh^+ ranges from 307.5 to 308.0 eV. In this case, the binding energy of Rh $3d_{5/2}$ of Rh_1/VO_2 was shifted to 309.9 eV (Figure 1F) owing to the strong metal–support interaction between single Rh atoms and the VO_2 nanorods.[14d,17] Moreover, the V species in Rh_1/VO_2 were determined to be in the V^{4+} state (Figure S3). Cl signals were not detected in the XPS measurements (Figure S4), suggesting that the Rh single atoms are present in a bare state.

The hydrolysis of NH_3BH_3 was performed to study how the metal–support interactions in Rh_1/VO_2 change upon the metal–insulator transition. The volume of the evolved gas was measured with a gas burette (Figure 2). Without a catalyst or with VO_2 nanorods as the catalyst, no gas was detected. The use of Rh_1/VO_2 led to the generation of a large amount of gas according to Equation (1):

$$NH_3BH_3 + 2H_2O \rightarrow NH_4^+ + BO_2^- + 3H_2 \quad (1)$$

The volume of H_2 was continuously measured to monitor the kinetics of the reaction. We investigated the catalytic performance of Rh_1/VO_2 at temperatures from 323.2 to 358.2 K with 2.5 K increments. As shown in Figure 2, about 120 mL of H_2 were generated within 10 min over Rh_1/VO_2 at all of these temperatures. The volume of generated H_2 was consistent with the theoretical amount of H_2 according to Equation (1), indicating the complete consumption of NH_3BH_3 in this process. As expected, the rate of H_2 generation increased with an increase in temperature. To quantitatively evaluate the catalytic activity, the turnover

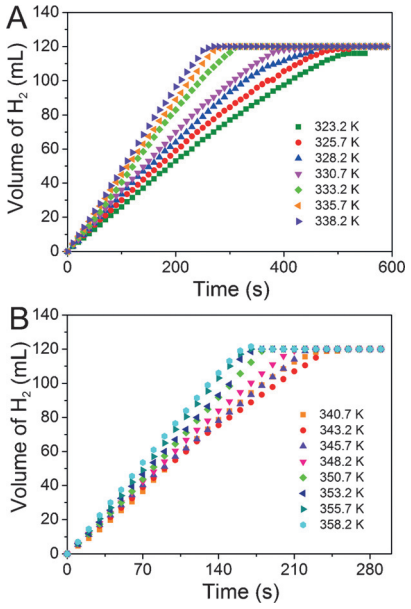

Figure 2. A, B) Time course of H_2 evolution from NH_3BH_3 using Rh_1/VO_2 single-atom catalysts at temperatures ranging from 323.2 to 338.2 K and from 340.7 to 358.2 K, respectively.

frequencies (TOFs) were calculated at different temperatures to construct an Arrhenius plot, showing the logarithmic TOF as a function of $1/T$ (Figure 3A). The TOF numbers were determined based on the slope of the reaction profile in the initial stage of the reaction (conversion $< 20\,\%$). The TOFs of Rh_1/VO_2 were 1.2 and 0.8 s^{-1} at 353.2 and 333.2 K, respectively, which are comparable to those of state-of-the-art

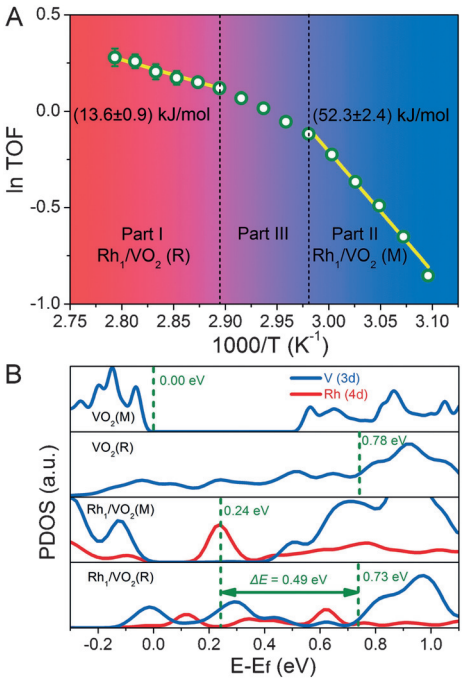

Figure 3. A) Arrhenius plot for NH_3BH_3 hydrolysis over Rh_1/VO_2. B) Calculated PDOS of VO_2(M), VO_2(R), Rh_1/VO_2(M), and Rh_1/VO_2(R). E_f represents the Fermi level of VO_2(M).

catalysts (Table S2).[10–12,18,19] Unlike the Arrhenius plots for hydrogen formation reactions over conventional catalysts, the current data points cannot be linearly fitted when the whole temperature region is considered. Interestingly, the data in part I (345.7–358.2 K) and part II (323.2–335.7 K) fit the linear plot well. Correspondingly, the activation energies for part I (E_{aI}) and part II (E_{aII}) were calculated as 13.6 ± 0.9 and 52.3 ± 2.4 kJ mol^{-1}, respectively. The region in between was regarded as the transition region, part III (335.7–345.7 K); as this temperature range is in good agreement with the phase-transition temperature of the support (337.2–344.2 K; Figure S2), we believe that the change in activation energy might be caused by the phase transition of VO_2. To support this hypothesis, Rh_1/C with individual Rh atoms dispersed on active carbon was synthesized as a reference compound; the dispersion of isolated Rh atoms was again confirmed by a HAADF-STEM image and EXAFS spectra (Figure S5 and Table S1). Rh_1/C was applied in NH_3BH_3 hydrolysis at temperatures from 323.2 to 358.2 K with 5.0 K increments (Figure S6A). According to the obvious linear Arrhenius behavior (Figure S6B), the apparent activation energy of Rh_1/C was 42.8 ± 1.4 kJ mol^{-1}. The difference in the catalytic behavior of Rh_1/VO_2 and Rh_1/C demonstrates that the variation in the apparent activation energy over Rh_1/VO_2 is related to the substrate.

To investigate the effect of the Rh mass loading on the catalytic performance, Rh_1/VO_2 single-atom catalysts with Rh mass loadings of 0.2 % and 0.8 % were also synthesized. We conducted the NH_3BH_3 hydrolysis over 100 mg of the Rh_1/VO_2 catalysts with different Rh loadings at 353.2 and 333.2 K. As the Rh loading was increased, the reaction rate increased, but the TOF number remained almost unchanged (Figures S7 and S8). This result demonstrates that single Rh atoms served as the active sites in NH_3BH_3 hydrolysis.

To investigate the stability of Rh_1/VO_2, we carried out a series of characterizations of the catalyst after NH_3BH_3 hydrolysis at 333.2 and 353.2 K. The HAADF-STEM images of Rh_1/VO_2 after the reactions showed that the Rh atoms were still atomically dispersed on the surface of the VO_2 nanorods (Figure S9A,B). In addition, the X-ray diffraction (XRD) patterns of Rh_1/VO_2 after the reactions could still be assigned to the monoclinic phase of VO_2 (Figure S9C). As shown in the XPS spectra, the binding energies of Rh and V in the used Rh_1/VO_2 system were identical to those in the as-prepared one, indicating the oxidized state of the single Rh atoms and the V^{4+} state for the V atoms (Figure S9D,E). Furthermore, we repeatedly reused the Rh_1/VO_2 catalyst to determine its catalytic stability. After five rounds of reaction at 333.2 and 353.2 K, more than 95 % of the original reactivity was preserved (Figures S10 and S11). Collectively, Rh_1/VO_2 displays high structural and catalytic stability.

According to previous studies on the hydrolysis of NH_3BH_3,[3,4,20] we propose two possible reaction pathways for this reaction (paths A and B; see the Experimental Section for a detailed discussion). In short, path A corresponds to the activation of a proton while path B describes the activation of both water and NH_3BH_3 molecules. To gain further insight into the reaction mechanism and determine the rate-limiting step, we conducted a set of experiments that involved changing the concentrations of NH_3BH_3 and H^+. When the reaction was carried out at different concentrations of NH_3BH_3 over Rh_1/VO_2 at 333.2 K and 353.2 K, the curves of the H_2 evolution with time overlapped at the initial stage of the reaction even though the overall amount of generated H_2 differs (Figure S12A,B). As such, the reaction rate and the corresponding TOF numbers remained stable with varied concentrations of NH_3BH_3 at a certain temperature (333.2 K or 353.2 K; Figure S12C), which rules out path B. To investigate the influence of the H^+ concentration, the pH value was varied by using phosphate buffer instead of the aqueous solution (Table S3). In the absence of catalyst, the generation of H_2 was below 1.5 mL at pH 6 to 8 after 20 min (Figure S13), indicating that the influence of H^+ or OH^- ions on the reaction rate is negligible under these reaction conditions. When Rh_1/VO_2 was added, the reaction rate clearly changed upon varying the pH value (Figure S12D,E). As shown in Figure S12F, the TOF number decreased from 1.1 to 0.6 s^{-1} and from 1.6 to 1.0 s^{-1} when the pH value was increased from 6.0 to 8.0 at 333.2 and 353.2 K, respectively, indicating a positive correlation between the H^+ concentration and the reaction rate. Consequently, the above results show that the activation of a proton is the rate-limiting step and that path A

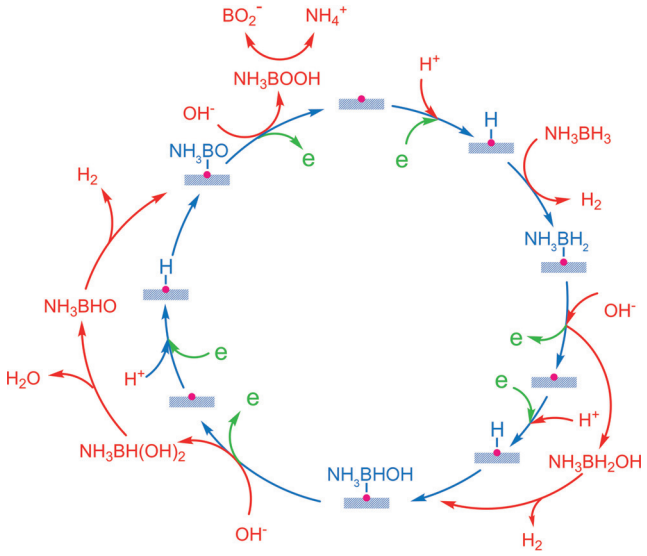

Figure 4. Proposed mechanism for NH_3BH_3 hydrolysis over Rh_1/VO_2.

is operating. The whole reaction process (path A) is depicted in Figure 4.

Based on the aforementioned discussion, a possible mechanism was proposed to understand the different apparent activation energies for the two phases of VO_2. The activation of a proton can be written as Equation (2):

$$H^+ + e + * \rightarrow H^* \quad (2)$$

In this case, $\mu(H^+)$, $\mu(e)$, and $\mu(H^*)$ would affect the apparent activation energy, where μ and * represent the chemical potential and a surface site, respectively. An insulator–metal phase transition of the substrate will induce changes in both $\mu(e)$ and $\mu(H^*)$ whereas $\mu(H^+)$ is expected to remain almost unchanged. As a result, $\mu(e)$, which corresponds to the highest occupied state of Rh in Rh_1/VO_2, plays a pivotal role in determining the difference between the apparent activation energies of the two phases of VO_2. To investigate the metal–support interactions, we performed first-principle calculations for pure VO_2 and Rh_1/VO_2. With the alignment of O 2s states, the projected densities of states (PDOS) of VO_2(M), VO_2(R), Rh_1/VO_2(M), and Rh_1/VO_2(R) are shown in Figure 3B. The Fermi level of VO_2(R) is located 0.78 eV above that of VO_2(M). When VO_2(M) is doped with Rh, new occupied states will arise in the band gap of VO_2(M) owing to the greater number of d electrons in Rh compared with V. For comparison, the highest occupied state of single Rh atoms supported on VO_2(R) is considered to be at an energy comparable to the Fermi level of VO_2(R) because of the low concentration of doped Rh as well as Rh and VO_2(R) both being in the metal phase. As expected, the highest occupied state of single Rh atoms supported on VO_2(M) was at 0.24 eV relative to the Fermi level of VO_2(M). Meanwhile, the highest occupied state of single Rh atoms supported on VO_2(R) was at 0.73 eV, similar to the Fermi level of VO_2(R). As H^+ ions need to take electrons from the catalyst to generate H* according to Equation (2), a high $\mu(e)$ value is favorable to accelerate the reaction. Therefore, the difference between the $\mu(e)$ values of Rh_1/VO_2(M) and Rh_1/VO_2(R) directly correlates with the difference in the apparent activation energies of these two systems. Taking the value of the in-gap state center as a reference, $\Delta\mu(e)$ was calculated to be 0.49 ± 0.10 eV (47.3 ± 9.6 kJ mol^{-1}) for Rh_1/VO_2(M) and Rh_1/VO_2(R), which is close to the difference of 38.7 ± 2.6 kJ mol^{-1} in the apparent activation energy (ΔE_a). From the perspective of electronic modulation, a hypothesis was previously reported for the metal–support interaction, where electron transfer from or to a support altered the charge state of the metal and therefore the catalytic performance.[21,22] In this work, we directly associated the catalytic performance of Rh_1/VO_2 with the highest occupied state of the single Rh atoms, which was determined by the band structure of the substrate.

Based on the above assumption that the catalytic properties can be manipulated by tuning the highest occupied state of the single Rh atoms, we surmised that several other metals should be active catalysts in NH_3BH_3 hydrolysis upon changing their highest occupied states. To support this point, we conducted a set of extensive experiments following a similar procedure except for replacing Rh with other metals, including Fe, Co, Ni, Cu, Ag, and Au, to form metal-doped nanocrystals, denoted as M_1/VO_2. All of the supported metals were shown to be present in oxidized states based on the XPS spectra (Figure S14). As expected, both noble and non-noble metal catalyst systems exhibited remarkable activity towards NH_3BH_3 hydrolysis (Table S2). According to the Arrhenius plots, there are obvious changes in the apparent activation energies of M_1/VO_2 that are induced by the phase transformation (Figure 5A), similar to the catalytic performance of Rh_1/VO_2. Figure 5B shows a systematic comparison of the differences in the apparent activation energies for part I and part II for different catalyst systems. In

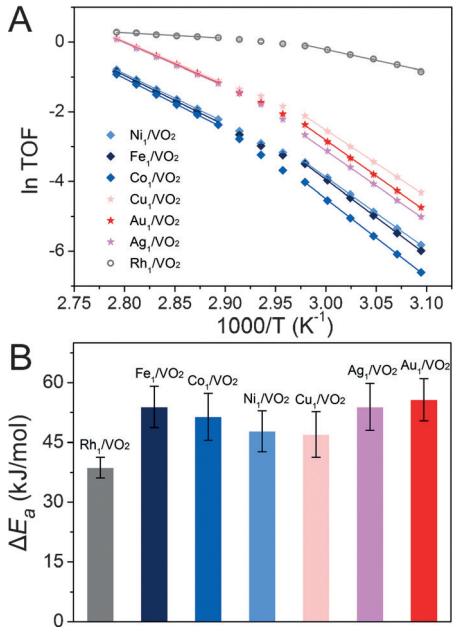

Figure 5. A) Arrhenius plots for NH_3BH_3 hydrolysis over Rh_1/VO_2, Fe_1/VO_2, Co_1/VO_2, Ni_1/VO_2, Cu_1/VO_2, Ag_1/VO_2, and Au_1/VO_2 and B) the corresponding ΔE_a values. ΔE_a represents the difference in the apparent activation energies of M_1/VO_2(M) and M_1/VO_2(R).

spite of the large discrepancies in catalytic activity and E_a between different catalysts, the ΔE_a values for all of these systems were roughly identical, ranging from 38.7 to 55.7 kJ mol^{-1} (Table S4). This result is reasonable based on our aforementioned mechanism, which associates the activation energy with the highest occupied state. The energy differences of the highest occupied states of single metal atoms supported on VO_2(M) and VO_2(R) range from 0.23 eV to 0.78 eV (22.2–75.2 kJ mol^{-1}); these values were estimated based on the gaps from the Fermi level of VO_2(R) to the valence-band maximum and the conduction-band minimum of VO_2(M), respectively. It is worth noting that the TOF numbers of VO_2 nanorods doped with non-noble metals are comparable to that of Rh_1/VO_2 at high temperatures (> 353.2 K), revealing significant activity for M_1/VO_2. Among these single-atom catalysts, Rh_1/VO_2 showed the lowest activation energy and the highest activity. The NH_3BH_3 hydrolysis could be approximately regarded as the zero-voltage equivalent of the hydrogen evolution reaction. Accordingly, the volcano curve for the activity and hydrogen adsorption energies could be adopted.[23] As indicated by the volcano curve, Rh is endowed with the optimal hydrogen adsorption energy and thus has the highest activity among the metals studied in this work.

In conclusion, a quantitative relationship between the catalytic performance and metal–support interactions was established in terms of the highest occupied state by using Rh_1/VO_2 single-atom catalysts in NH_3BH_3 hydrolysis. Based on the proposed influence of the metal–support interaction, remarkably high catalytic activities towards the hydrolysis of NH_3BH_3 were achieved with other metals, even non-noble metals, by changing the highest occupied states of the catalysts. This work provides a guideline for the rational design of efficient and inexpensive catalysts towards hydrogen generation by controlling the band structures of the catalysts.

Acknowledgements

This work was supported by the National Synchrotron Radiation Laboratory, the Collaborative Innovation Center of Suzhou Nano Science and Technology, MOST of China (2014CB932700), the NSFC (21373259, 21203099, 21573206, and 51371164), the Key Research Program of Frontier Sciences of the CAS (QYZDB-SSW-SLH017), the Strategic Priority Research Program of the CAS (XDB01020000 and XDA09030102), the Doctoral Fund of Ministry of Education of China (20120031120033), the Research Program for Advanced and Applied Technology of Tianjin (13JCYBJC36800), the Fok Ying Tung Education Foundation (151008), Fundamental Research Funds for the Central Universities, and the Hundred Talents project of the CAS.

Conflict of interest

The authors declare no conflict of interest.

Keywords: hydrolysis · metal–support interactions · rhodium · single-atom catalysts · vanadium dioxide

How to cite: *Angew. Chem. Int. Ed.* **2017**, *56*, 4712–4718
Angew. Chem. **2017**, *129*, 4790–4796

[1] a) L. V. Mattos, G. Jacobs, B. H. Davis, F. B. Noronha, *Chem. Rev.* **2012**, *112*, 4094–4123; b) E. Balaraman, E. Khaskin, G. Leitus, D. Milstein, *Nat. Chem.* **2013**, *5*, 122–125; c) R. Rousseau, D. A. Dixon, B. D. Kay, Z. Dohnalek, *Chem. Soc. Rev.* **2014**, *43*, 7664–7680; d) W. Guo, D. G. Vlachos, *Nat. Commun.* **2015**, *6*, 8619.

[2] T. C. Johnson, D. J. Morris, M. Wills, *Chem. Soc. Rev.* **2010**, *39*, 81–88.

[3] J. Choi, A. H. R. MacArthur, M. Brookhart, A. S. Goldman, *Chem. Rev.* **2011**, *111*, 1761–1779.

[4] G. Alcaraz, S. Sabo-Etienne, *Angew. Chem. Int. Ed.* **2010**, *49*, 7170–7179; *Angew. Chem.* **2010**, *122*, 7326–7335.

[5] M. Nielsen, E. Alberico, W. Baumann, H. J. Drexler, H. Junge, S. Gladiali, M. Beller, *Nature* **2013**, *495*, 85–89.

[6] M. Grasemann, G. Laurenczy, *Energy Environ. Sci.* **2012**, *5*, 8171–8181.

[7] W. Chen, J. Ji, X. Feng, X. Duan, G. Qian, P. Li, X. Zhou, D. Chen, W. Yuan, *J. Am. Chem. Soc.* **2014**, *136*, 16736–16739.

[8] H. Cheng, X. Qian, Y. Kuwahara, K. Mori, H. Yamashita, *Adv. Mater.* **2015**, *27*, 4616–4621.

[9] H. Ma, C. Na, *ACS Catal.* **2015**, *5*, 1726–1735.

[10] Q. L. Zhu, J. Li, Q. Xu, *J. Am. Chem. Soc.* **2013**, *135*, 10210–10213.

[11] a) X. Xia, L. Figueroa-Cosme, J. Tao, H. C. Peng, G. Niu, Y. Zhu, Y. Xia, *J. Am. Chem. Soc.* **2014**, *136*, 10878–10881; b) Y. Chen, Q. L. Zhu, N. Tsumori, Q. Xu, *J. Am. Chem. Soc.* **2015**, *137*, 106–109; c) W. Y. Yu, G. M. Mullen, D. W. Flaherty, C. B. Mullins, *J. Am. Chem. Soc.* **2014**, *136*, 11070–11078; d) Q. Y. Bi, X. L. Du, Y. M. Liu, Y. Cao, H. Y. He, K. N. Fan, *J. Am. Chem. Soc.* **2012**, *134*, 8926–8933.

[12] C. Y. Peng, L. Kang, S. Cao, Y. Chen, Z. S. Lin, W. F. Fu, *Angew. Chem. Int. Ed.* **2015**, *54*, 15725–15729; *Angew. Chem.* **2015**, *127*, 15951–15955.

[13] a) X. F. Yang, A. Wang, B. Qiao, J. Li, J. Liu, T. Zhang, *Acc. Chem. Res.* **2013**, *46*, 1740–1748; b) K. Iwase, T. Yoshioka, S. Nakanishi, K. Hashimoto, K. Kamiya, *Angew. Chem. Int. Ed.* **2015**, *54*, 11068–11072; *Angew. Chem.* **2015**, *127*, 11220–11224; c) G. Vilé, D. Albani, M. Nachtegaal, Z. P. Chen, D. Dontsova, M. Antonietti, N. López, J. Pérez-Ramírez, *Angew. Chem. Int. Ed.* **2015**, *54*, 11265–11269; *Angew. Chem.* **2015**, *127*, 11417–11422; d) P. Chen, T. Zhou, L. Xing, K. Xu, Y. Tong, H. Xie, L. Zhang, W. Yan, W. Chu, C. Wu, Y. Xie, *Angew. Chem. Int. Ed.* **2017**, *56*, 610–614; e) H. Zhang, J. Wei, J. Dong, G. Liu, L. Shi, P. An, G. Zhao, J. Kong, X. Wang, X. Meng, J. Zhang, J. Ye, *Angew. Chem. Int. Ed.* **2015**, *54*, 14308–14312; *Angew. Chem.* **2015**, *127*, 14516–14520.

[14] a) W. Huang, S. Zhang, Y. Tang, Y. Li, L. Nguyen, Y. Li, J. Shan, D. Xiao, R. Gagne, A. I. Frenkel, F. Tao, *Angew. Chem. Int. Ed.* **2016**, *55*, 13441–13445; *Angew. Chem.* **2016**, *128*, 13639–13643; b) P. Yin, T. Yao, Y. Wu, L. Zheng, Y. Lin, W. Liu, H. Ju, J. Zhu, X. Hong, Z. Deng, G. Zhou, S. Wei, Y. Li, *Angew. Chem. Int. Ed.* **2016**, *55*, 10800–10805; *Angew. Chem.* **2016**, *128*, 10958–10963; c) S. Yang, J. Kim, Y. J. Tak, A. Soon, H. Lee, *Angew. Chem. Int. Ed.* **2016**, *55*, 2058–2062; *Angew. Chem.* **2016**, *128*, 2098–2102; d) L. Wang, W. Zhang, S. Wang, Z. Gao, Z. Luo, X. Wang, R. Zeng, A. Li, H. Li, M. Wang, X. Zheng, J. Zhu, W. Zhang, C. Ma, R. Si, J. Zeng, *Nat. Commun.* **2016**, *7*, 14036; e) B. Qiao, A. Wang, X. Yang, L. F. Allard, Z. Jiang, Y. Cui, J. Liu, J. Li, T. Zhang, *Nat. Chem.* **2011**, *3*, 634–641.

[15] a) A. Zylbersztejn, N. F. Mott, *Phys. Rev. B* **1975**, *11*, 4383 – 4395; b) C. Wu, X. Zhang, J. Dai, J. Yang, Z. Wu, S. Wei, Y. Xie, *J. Mater. Chem.* **2011**, *21*, 4509 – 4517.
[16] S. J. Pennycook, D. E. Jesson, *Ultramicroscopy* **1991**, *37*, 14 – 38.
[17] S. Ida, N. Kim, E. Ertekin, S. Takenaka, T. Ishihara, *J. Am. Chem. Soc.* **2015**, *137*, 239 – 244.
[18] a) G. Chen, S. Desinan, R. Nechache, R. Rosei, F. Rosei, D. Ma, *Chem. Commun.* **2011**, *47*, 6308 – 6310; b) K. Mori, K. Miyawaki, H. Yamashita, *ACS Catal.* **2016**, *6*, 3128 – 3135; c) H. Yen, Y. Seo, S. Kaliaguine, F. Kleitz, *ACS Catal.* **2015**, *5*, 5505 – 5511; d) J. Manna, S. Akbayrak, S. Özkar, *Appl. Catal. B* **2017**, *208*, 104 – 115; e) R. Fernandes, N. Patel, R. Edla, N. Bazzanella, D. C. Kothari, A. Miotello, *Appl. Catal. A* **2015**, *495*, 23 – 29; f) H. L. Wang, J. M. Yan, Z. L. Wang, Q. Jiang, *Int. J. Hydrogen Energy* **2012**, *37*, 10229 – 10235.
[19] a) N. Cao, J. Su, W. Luo, G. Cheng, *Int. J. Hydrogen Energy* **2014**, *39*, 426 – 435; b) N. Cao, K. Hu, W. Luo, G. Cheng, *J. Alloys Compd.* **2014**, *590*, 241 – 246; c) O. Akdim, U. B. Demirci, P. Miele, *Int. J. Hydrogen Energy* **2013**, *38*, 5627 – 5637; d) Q. Yao, Z. H. Lu, W. Huang, X. Chen, J. Zhu, *J. Mater. Chem. A* **2016**, *4*, 8579 – 8583; e) Z. L. Wang, J. M. Yan, H. L. Wang, Q. Jiang, *J. Power Sources* **2013**, *243*, 431 – 435.
[20] T. W. Graham, C. W. Tsang, X. Chen, R. Guo, W. Jia, S. M. Lu, C. Sui-Seng, C. B. Ewart, A. Lough, D. Amoroso, K. Abdur-Rashid, *Angew. Chem. Int. Ed.* **2010**, *49*, 8708 – 8711; *Angew. Chem.* **2010**, *122*, 8890 – 8893.
[21] V. E. Henrich, P. A. Cox, *The Surface Science of Metal Oxides*, Cambridge University Press, Cambridge, **1996**.
[22] C. T. Campbell, *Nat. Chem.* **2012**, *4*, 597 – 598.
[23] a) S. J. Trasatti, *Electroanal. Chem.* **1972**, *39*, 163 – 184; b) J. K. Nørskov, T. Bligaard, A. Logadottir, J. R. Kitchin, J. G. Chen, S. Pandelov, U. Stimming, *J. Electrochem. Soc.* **2005**, *152*, J23 – J26.

Manuscript received: January 31, 2017
Revised: March 1, 2017
Final Article published: March 30, 2017

